Immune profiling and tracking of two-dimensional transition metal dichalcogenides in cells and tissues

Arianna Gazzi [a,1], Laura Fusco [a,b,1], Marco Orecchioni [c], Sandeep Keshavan [d], Yuyoung Shin [e], Jean-Charles Grivel [f], Darawan Rinchai [b], Eiman I. Ahmed [b], Ofer Elhanani [g], Giulia Furesi [h], Martina Rauner [i], Leeat Keren [g], Klaus Ley [c,j], Cinzia Casiraghi [e], Davide Bedognetti [b,k,l,*], Bengt Fadeel [d], Lucia Gemma Delogu [m,a,**]

[a] ImmuneNano Laboratory, Department of Biomedical Sciences, University of Padua, Padua, Italy
[b] Translational Medicine Department, Sidra Medicine, Doha, Qatar
[c] La Jolla Institute for Allergy and Immunology, San Diego, CA, USA
[d] Division of Molecular Toxicology, Institute of Environmental Medicine, Karolinska Institutet, Stockholm, Sweden
[e] Department of Chemistry, University of Manchester, Manchester, UK
[f] Advanced Cell Therapy Core, Sidra Medicine, Doha, Qatar
[g] Department of Molecular Cell Biology, Weizmann Institute of Science, Rehovot, Israel
[h] School of Medicine, Washington University, St. Louis, MO, USA
[i] Department of Medicine III, Center for Healthy Aging, Technische Universität Dresden, Dresden, Germany
[j] Immunology Center of Georgia (IMMCG), Augusta University, Augusta, CA, USA
[k] Department of Internal Medicine and Medical Specialties, University of Genoa, Genoa, Italy
[l] College of Health and Life Sciences, Hamad Bin Khalifa University, Doha, Qatar
[m] Department of Biology, College of Arts and Sciences, Khalifa University, Abu Dhabi, United Arab Emirates

ARTICLE INFO

ABSTRACT

Two-dimensional (2D) transition metal dichalcogenides (TMDs), such as molybdenum disulfide (MoS_2) and tungsten disulfide (WS_2), have attracted considerable interest in biomedicine due to their unique combination of physicochemical properties. The effect of nanomaterials on immune cells and their biodistribution are critical aspects of their clinical translation. However, understanding the interactions of these emerging 2D nanomaterials with the complex pool of peripheral blood mononuclear cells (PBMCs) at the single-cell level and their in situ localization in the main organs still needs to be discovered, preventing their translation in medical settings. Here, we report in-depth immune profiling of water-based and defect-free 2D formulations of MoS_2 and WS_2 through the simultaneous label-free tracking of their immune cell interactions, both ex vivo in human PBMCs and in vivo in mice by high-dimensional analytical approaches, as well as their biodistribution. For comparison, we studied graphene, the hitherto most explored 2D material for biomedical applications. First, we assessed the impact at the protein and gene level by multiplex protein arrays and RNA sequencing, demonstrating a very modest effect of MoS_2 and WS_2 on immune cell functionality compared to graphene. Then, a single-cell view of the effects of MoS_2 and WS_2 on 16 primary human immune cell types in terms of viability and functionality was obtained by single-cell mass cytometry by time-of-flight (CyTOF). We explored over 30 markers looking at multiple cell parameters. Finally, we present evidence that MoS_2 and WS_2 are visible, without the need for labeling, at the single-cell and tissue level by CyTOF, imaging mass cytometry, and multiplexed ion beam imaging by time-of-flight (MIBI-TOF). In particular, MoS_2 and WS_2 could be detected in the molybdenum (^{95}Mo) and tungsten ($^{180-186}W$) channels, respectively, which are not used for commercial mass cytometry tags, allowing for the simultaneous interrogation of a wide variety of biological parameters ex vivo and in vivo following intravenous administration of the TMDs. Indeed, we demonstrated the accumulation of TMDs in the main organs by MIBI-TOF and they could also be identified in specific immune cell subsets by CyTOF. Among the two TMDs studied, WS_2 exhibited the highest brightness and signal intensity in all the cell subpopulations and tissues analyzed.

In conclusion, we identified TMDs as immune-compatible nanoplatforms, traceable at the single-cell and tissue (sub-organ) levels, thus opening up new perspectives for their exploration in biomedicine.

Introduction

Two-dimensional (2D) transition metal dichalcogenides (TMDs) [1], such as molybdenum disulfide (MoS_2) and tungsten disulfide (WS_2), are a new class of inorganic graphene-like nanomaterials [2]. The intriguing physical and chemical characteristics of TMDs have led to the rapid development of research on these emerging materials for promising applications in biomedicine, including drug delivery, tissue engineering, cancer therapy, and bioimaging [3–6]. Assessing the biosafety profiles of nanomaterials is critical to take advantage of their potential in biomedicine [5,7,8].

Previous studies have shown that MoS_2 and WS_2 have greater biocompatibility compared to pristine graphene and its analogs [9] even though aggregated MoS_2 exerted higher cytotoxicity when compared to 2D MoS_2 [10,11]. Despite these initial studies, there is a lack of knowledge on the impact of TMDs ex vivo on the complex pool of primary blood immune cells [12–16]. In fact, so far, most of the studies were carried out only on one immune cell type at a time or using immortalized cell lines. Therefore, before their biomedical application, a thorough evaluation of their toxicity and immune profiling are mandatory.

In this context, we have recently found that MoS_2 triggered trained immunity in primary human macrophages through epigenetic and metabolic pathways, without any signs of cytotoxicity [12]. Lin H. et al. demonstrated that MoS_2 exerted little toxicity towards macrophages, even though it could trigger cell stress and inflammation [13]. Similarly, MoS_2 showed no toxicity in dendritic cells [14] and RAW 264.7 cells after their internalization, but a strong pro-inflammatory and pro-fibrogenic response was induced by aggregated MoS_2 in THP-1 cells [16]. Others have shown that PEG-functionalized MoS_2 sheets induced cytokine secretion in murine macrophages [17], while few-layered MoS_2 enhanced dendritic cell (DC) maturation and T cell stimulation [18]. On the other hand, WS_2 could trigger macrophage activation indirectly through the induction of reactive oxygen species production in neighboring lung cells [19].

Immune cell interactions are pivotal in driving future TMD applications. Indeed, TMDs demonstrated promising applications in photothermal therapy showing interactions of the materials with immune cells in the tumor microenvironment. In particular, multifunctional MoS_2-based nanotools for antitumor immunotherapy could directly trigger host immunity by activating the antigen-specific T cells [20] and, when functionalized with cytosine–phosphate–guanine, the nanoplatform could stimulate the production of proinflammatory cytokines, remarkably triggering the immune response [21]. A reduction of cancer cell proliferation when co-cultured with a macrophage-like cell upon near-infrared irradiation was also observed. These studies were all carried out using a single immune cell type (mostly macrophages) while here we assessed their impact on up to 16 immune cell types. Furthermore, different results can be attributed to the starting physicochemical properties of the TMDs, as each preparation method gives nanosheets with different lateral size and thickness distributions as well as charge and surface chemistry, making the comparison between different studies very challenging. In addition, there is a lack of knowledge concerning the immune impact of both MoS_2 and WS_2 compared to graphene. Filling this knowledge gap will be fundamental to advance in their biomedical translation.

Therefore, there is an unmet need for a systematic and comprehensive approach, based on well-characterized 2D materials, addressing the complex pool of primary human immune cell subpopulations that exist in the blood. Furthermore, the detection of TMDs in cells and tissues with the simultaneous interrogation of several biological and immunological parameters is required to significantly expand their potential biomedical applications. These scientific needs can be met only by novel high-dimensional approaches, such as single-cell mass cytometry by time-of-flight (CyTOF), imaging mass cytometry (IMC), and multiplexed ion beam imaging by time-of-flight (MIBI-TOF). CyTOF represents one of the most powerful tools available for immune phenotyping. This technology relies on mass cytometry to detect metal element-tagged antibodies based on their mass/charge ratio (m/z), with minimal overlap or background noise [22], thus increasing multiplexing capabilities, specificity, and sensitivity over common fluorescence-based approaches such as flow cytometry and fluorescence imaging [23]. While CyTOF only applies to cells in suspension, IMC [23, 24] and MIBI-TOF [25] are imaging platforms that similarly use elementally labeled probes to measure dozens of molecular parameters at single-cell resolution in situ. These three systems are unique in revealing a multitude of biological information in-depth and at a single-cell level, on several immune cell types and tissues, and could therefore provide new knowledge on TMDs.

CyTOF was previously applied to study Ag nanoparticle [26] uptake and for the detection of functionalized graphene [27]. We introduced this technology to detect label-free 2D transition metal-based materials (MXenes) at the single-cell level to reveal their interactions with the immune cells [28]. The understanding of the specific effects of nanomaterials on the different immune cell subpopulations is critical not only for their safety but also for the development of new advanced biomedical strategies. For instance, in the case of MXenes, Yan W et al. demonstrated that the materials could reduce the activation of allogeneic lymphocytes, highlighting their potential in the treatment of allograft vasculopathy and inflammatory diseases [29]. However, these high-dimensional methods have not been used to study TMDs, and their label-free in vivo tracking has never been shown before.

Here, we report in-depth immune profiling, label-free detection, and biodistribution of water-based and defect-free formulations of MoS_2 and WS_2 ex vivo and in vivo (Fig. 1). Graphene (G) formulation, prepared with the same method [30,31], was also tested as a reference material. Initially, we evaluated the immunocompatibility of MoS_2 and WS_2 ex vivo on human macrophages and peripheral blood mononuclear cells (PBMCs) and explored their impact on this complex pool of primary cells at the protein and gene level by multi-plex array and next-generation sequencing. Subsequently, our single-cell analysis dissected the extensive functional heterogeneity of the immune cell interactions of TMDs by simultaneously analyzing sixteen immune cell subpopulations ex vivo with CyTOF and IMC [32]. Then, we took advantage of MoS2 and WS_2 transition metal-based composition to detect the materials at the single-cell and tissue levels by CyTOF, IMC, and MIBI-TOF. In fact, while graphene requires laborious functionalization to enable its detection within the mass cytometry range of 75–209 Da [33,34], which could affect the material biocompatibility and biodistribution, we demonstrated that MoS_2 and WS_2 are visible by CyTOF as they allowed mass detection without the need for functionalization, in the molybdenum (^{95}Mo) and tungsten ($^{180–186}W$) channels, respectively. Therefore, we could detect the materials at the single-cell level in sixteen different primary human immune cell subpopulations by CyTOF and IMC, at the same time interrogating several biological parameters. Finally, we performed a pilot study in mice and revealed material biodistribution at the single-cell and tissue levels in the main organs by MIBI-TOF upon i.v. injection. This novel approach, allowing for the label-free detection of the materials at the single-cell and tissue levels, is expected to open up exciting new possibilities for TMDs in biomedicine.
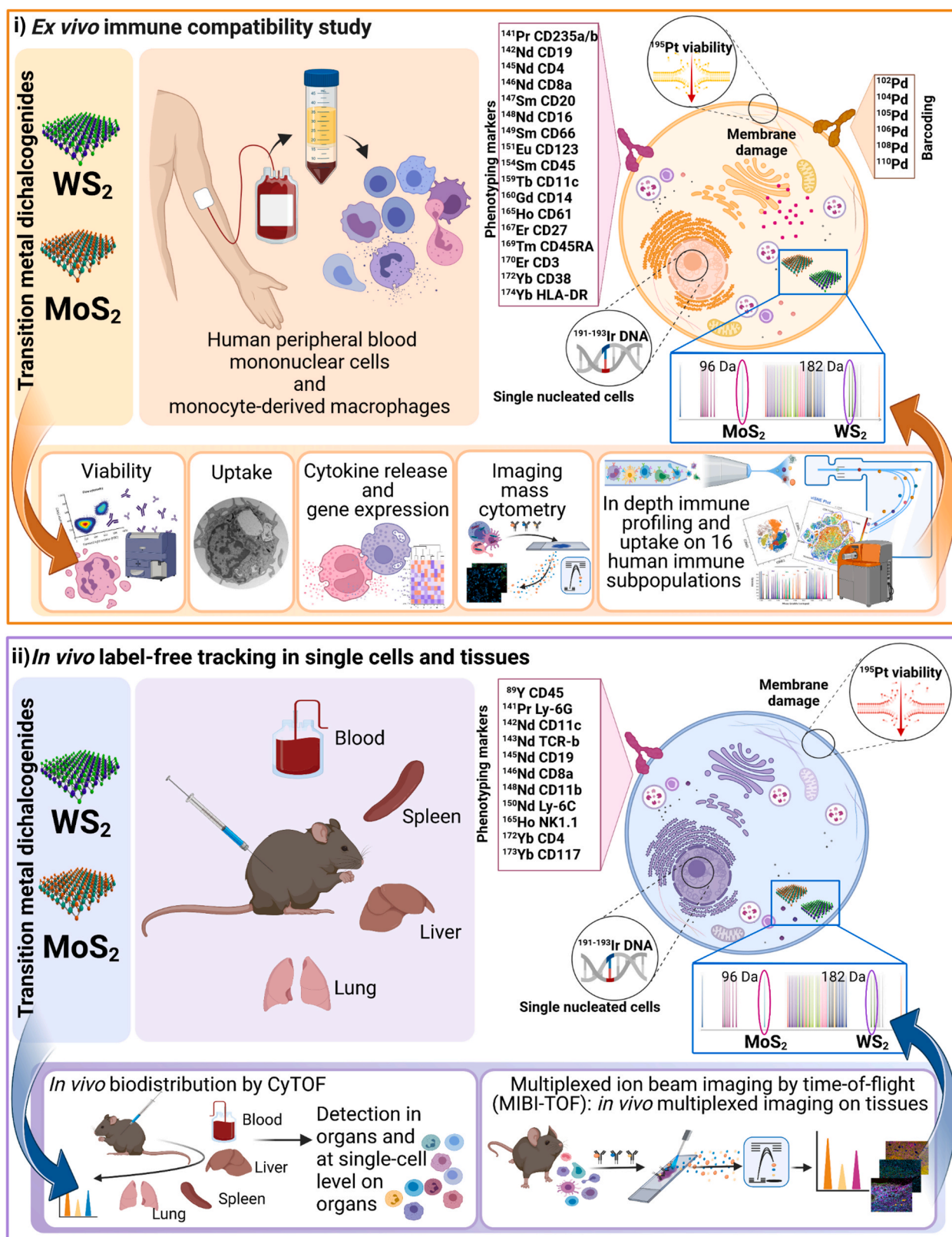
Fig. 1. Workflow of the study. Schematic representation for MoS_2 and WS_2 detection in cells and tissues using mass cytometry-based detection of stable isotope masses from 75 to 209 Da. **i)** Study workflow showing basic biological characterization of TMDs on whole blood and peripheral blood mononuclear cells. The impact of TMDs was assessed ex vivo on 16 human immune cell types by single-cell mass cytometry and imaging mass cytometry. Graphical representation of all metal tags used for single-cell mass cytometry experiments assessing immune cell phenotyping markers (pink box), viability, palladium-based barcoding (orange), and DNA staining. MoS_2 and WS_2 were detected in the ^{95}Mo and ^{182}W channels, respectively. **ii)** TMD in vivo testing from biodistribution to in vivo cell interactions by single-cell mass cytometry and multiplexed ion beam imaging.

Results and discussion

Physicochemical characterization of G, MoS$_2$, and WS$_2$

Water-based and defect-free G and TMDs formulations were prepared by liquid-phase exfoliation via non-covalent functionalization with 1-pyrenesulfonic acid sodium salt, as previously described [30,31]. The physicochemical properties of all materials have been fully characterized (Fig. S1a-g, Table S1h). Both G and TMD formulations were defect-free and had the same surface charge type (negative) and chemistry, being produced by non-covalent functionalization with the same type of stabilizer [35]. However, G and the TMD nanosheets had different size and thickness distributions (Table S1h). In particular, G nanosheets, had a lateral size of ≈ 170 nm, and an average thickness of ≈ 6 nm, while MoS$_2$ and WS$_2$ had a lateral size of ≈ 40 and ≈ 50 nm, respectively, and a thickness between 4 and 7 nm [36]. AFM images and further information on surface topography can be found in Ref. 36. Assuming a thickness of 1–1.5 nm for a single layer, and taking into account the adsorbed stabilizer on both sides of the nano-sheet [36], the average number of layers was between 3 and 7, in good agreement with TEM results [37,38].

Care was taken to ensure that the materials were endotoxin-free as this may otherwise confound the results, particularly when analyzing their impact on the immune system [12]. To this end, the materials were evaluated for potential endotoxin contamination by the TNF-α expression test (TET) [39,40]. The TET assay is based on TNF-α expression in primary human monocyte-derived macrophages (HMDMs) exposed to a sub-cytotoxic concentration of the tested materials in the presence or absence of the endotoxin inhibitor, polymyxin B sulfate (Poly-B). The obtained results demonstrated that all materials were endotoxin-free (Fig. S1i). To determine the sub-cytotoxic concentration for endotoxin contamination testing, HMDMs were exposed to different concentrations (1–100 μg/mL) of G, MoS$_2$, or WS$_2$ for 24 h, and cell viability was evaluated by the LDH assay. As shown in Fig. S2a-c, no toxicity was observed in cells exposed to the 2D materials up to 100 μg/mL. Our data align with previous findings showing that TMDs did not affect the cell viability of murine macrophages [41]. Besides enabling endotoxin detection, the TET assay is also suggested as a suitable method for assessing the intrinsic inflammogenic properties of nanomaterials [39]. In this regard, the TET analysis revealed that neither G, MoS$_2$, or WS$_2$ triggered any pro-inflammatory TNF-α secretion in primary human macrophages (Fig. S1i).

We also evaluated the ability of G, MoS$_2$, and WS$_2$ to trigger the production of interleukin (IL)-1β, a hallmark of inflammasome activation, in HMDMs with or without priming with bacterial lipopolysaccharide (LPS) [42]. To this end, HMDMs were pre-incubated for 2 h with zVAD-FMK or MCC950, specific pan-caspase, and NLRP3 inhibitors, respectively, followed by 24 h exposure to the intermediated sub-cytotoxic concentration of 25 μg/mL of G, MoS$_2$, or WS$_2$. None of the 2D materials elicited IL-1β production in non-primed cells (Fig. S2d-f). LPS alone prompted IL-1β release, while no increase in IL-1β production was noted in LPS-primed cells treated with the 2D materials compared to primed cells.

Internalization of TMDs in primary human macrophages cultured ex vivo

To investigate the material–cell interactions, we performed transmission electron microscopy (TEM) analysis after exposure of HMDMs to 25 μg/mL of G, MoS$_2$, or WS$_2$ for 24 h. All the materials were readily internalized with no ultrastructural signs of cell death. They were found either as tightly packed 'bundles' in the cytoplasm or large cytoplasmic vacuoles, while none were found in the cell nucleus (Fig. S3). In particular, WS$_2$ and MoS$_2$ were mainly located in large vacuoles, as seen in Fig. S3d-i. On the other hand, G did not appear to trigger the formation of such vacuoles but rather 'bundles' of material dispersed throughout the cytoplasm (Fig. S3a-c). No signs of autophagic vacuoles

were seen. Our results align with previous studies demonstrating the uptake of MoS$_2$ by human monocyte-like THP-1 cells and murine macrophage-like RAW264.7 cells [41,43].

*Biocompatibility and immunocompatibility of TMDs*

Macrophages are tissue-resident cells. To deepen our understanding of the immunological impact of TMDs, we evaluated their effects on the complex pool of human PBMCs present in the blood. As observed for HMDMs, both MoS$_2$ and WS$_2$ were successfully internalized by PBMCs (Fig. 2a) and found in large aggregation and giant vacuoles inside the cells. The uptake of TMDs did not impair cell integrity, and no ultrastructural signs of autophagy or cell death were observed. We then explored the impact of the materials on cell viability. PBMCs were exposed to different concentrations (25–100 μg/mL) of G, MoS$_2$, or WS$_2$ for 24 h, and the percentage of dead cells was evaluated by flow cytometry. As observed for HMDMs, the materials did not impact the cell viability of total PBMCs at any concentration tested (Fig. 2b-d and Fig. S4). Taken together, these results are in agreement with the limited data available in the literature so far, showing that MoS$_2$- and WS$_2$-based materials do not induce cytotoxic effects in human cell lines [30,44], nor in primary murine bone marrow-derived dendritic cells [10,18], or primary HMDMs [20] (and the present study, see above).

Multiplex-based arrays for cytokine profiling of PBMCs exposed to TMDs

Subsequently, to further investigate the immune impact of the materials, we exposed PBMCs to 50 μg/mL of G, MoS$_2$, or WS$_2$ for 6 and 24 h and applied a multi-plex array for the detection of a comprehensive panel of forty secreted cytokines and chemokines. As positive controls, cells were exposed to concanavalin A (ConA, 10 μg/mL) or LPS (2 μg/mL). Heat maps represent the median expression values of the inflammatory mediators analyzed in the pool of PBMCs after treatment with the materials (Fig. 3 and Table S1). Individual cytokines were colored according to z-scored normalized value (blue = down-regulated, yellow square = unmodulated cytokines, red = up-regulated cytokines). Corresponding fold regulation and *p*-value are also reported. The obtained results showed that G significantly triggered the release of almost all the analyzed cytokines, inducing an effect comparable to that of the positive controls LPS and ConA. On the contrary, MoS$_2$ and WS$_2$ had a limited impact, significantly increasing only a few of the selected inflammatory mediators. Overall, MoS$_2$ exerted a higher effect than WS$_2$. In detail, MoS$_2$ and WS$_2$ enhanced the production of 13 and 1 cytokines, respectively. The two materials also showed a suppressive effect, inhibiting the release of 4 and 1 cytokines, respectively. In particular, significant production of C-X-C motif chemokine ligand (CXCL)1, CXCL2, and CXCL8, as well as C-C motif chemokine ligand (CCL)7, CCL8, CCL13, CCL19, CCL21, CCL25, and CCL26 was found following MoS$_2$ treatment, but to a lesser degree than for the G-exposed samples. MoS$_2$ also exerted a moderate pro-inflammatory effect substantiated by the increase of monocyte/myeloid chemoattractant protein CCL2, MI, CXCL8, and CXCL1. In addition, the production of interferon (IFN)γ, a primary activator of macrophages, was significantly increased only by MoS$_2$ and not by WS$_2$. Interestingly, MoS$_2$ significantly inhibited the production of CXCL10, CCL22, and CCL11, consistent with a reduction of the innate-adaptive immune response crosstalk [45,46]. On the other hand, WS$_2$ appeared to have an overall neutral effect, significantly increasing only the production of monocyte chemoattractant protein CCL2. However, also in this case, MoS$_2$ exerted a higher increase of this chemokine than WS$_2$. Similarly, WS$_2$ also had a limited suppressive effect inhibiting only the chemokine (C-C motif) ligand (CCL) 24 (CCL24), an eosinophil chemotactic protein. The secretion of IL-6, TNFα, and IL-1β remained unchanged, as reported previously in human bronchial epithelial cells [47]. On the other hand, previous studies have reported the increase of the same pro-inflammatory cytokines after TMD interaction with murine macrophages and DCs [17,18,48]. This difference in the immune
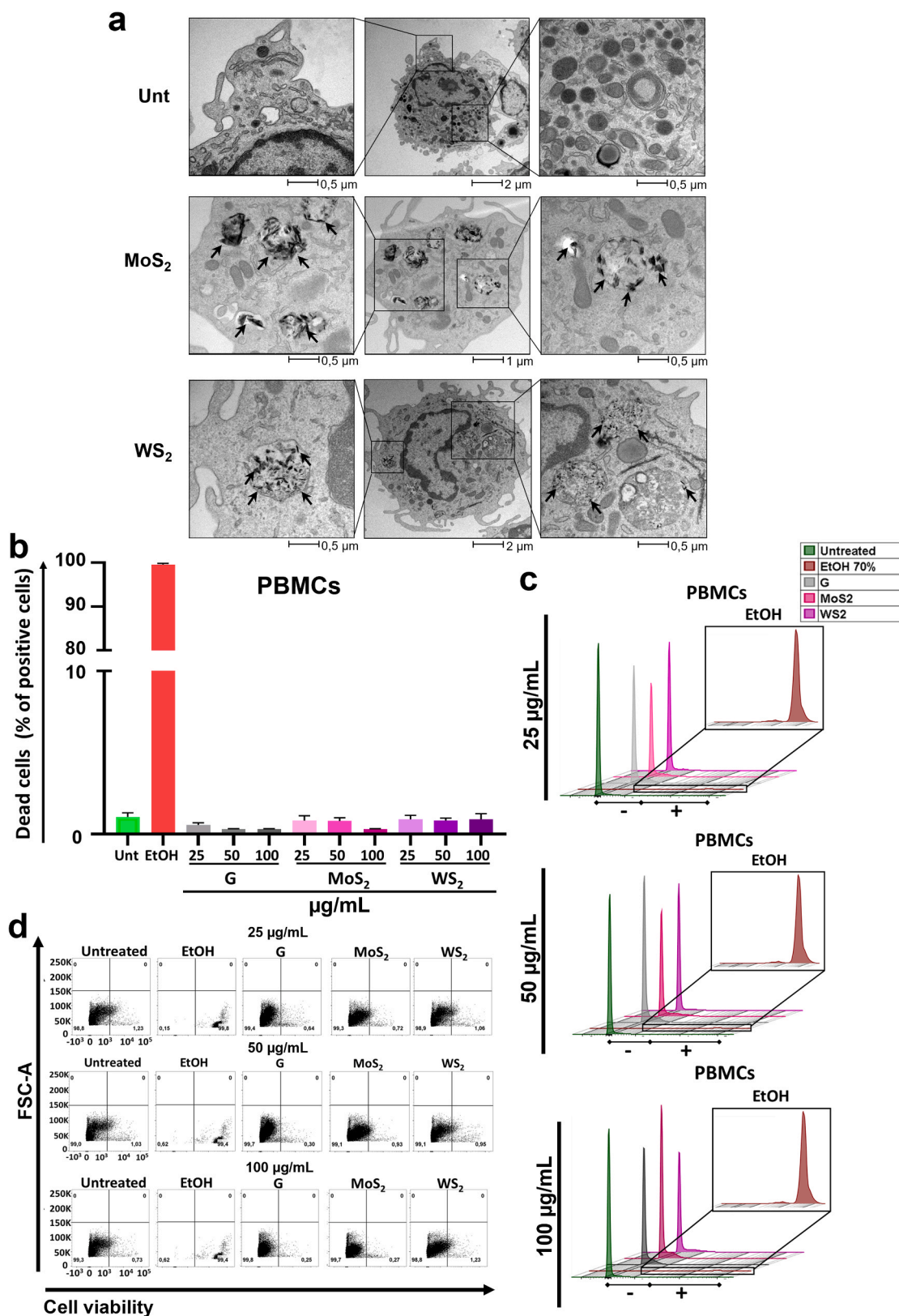
Fig. 2. Analysis of cell viability on PBMCs. a) Representative TEM images of MoS_2 and WS_2 interactions with PBMCs. Cells were incubated with MoS_2 or WS_2 (50 µg/mL) for 24 h. Arrows in higher magnification micrographs indicate internalized MoS_2 and WS_2. As shown in the panel, the representative images depict large aggregation and giant vacuoles inside the cells. Scale bars: 0.5, 1, and 2 µm. b) PBMCs were treated with different concentrations (25, 50, and 100 µg/mL) of G, MoS_2, or WS_2 for 24 h or left untreated (Unt). EtOH 70 % was used as a positive control. PBMCs were stained with live/dead Zombie Green dye, and cell death was evaluated and expressed as % of positive cells. c-d) Dot and histogram plots showing positivity for Zombie Green staining in PBMCs treated with G, MoS_2, or WS_2 (25, 50, and 100 µg/mL). Data are presented as mean ± SD of three independent samples. Comparison between groups was performed by one-way ANOVA, followed by Tukey's post hoc multiple comparison.
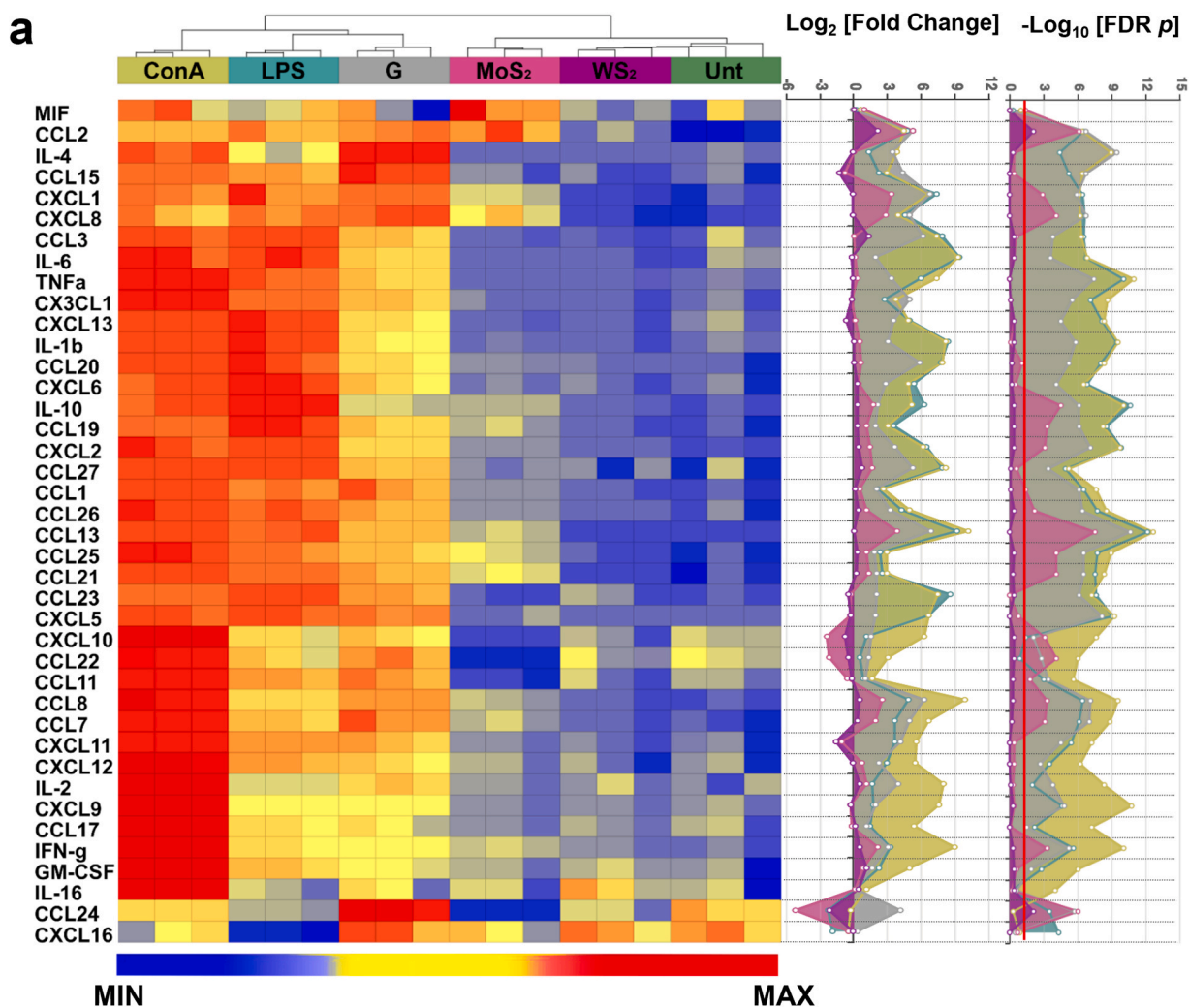
Fig. 3. Cytokine analysis on human peripheral blood mononuclear cells (PBMCs). Hierarchical cluster analysis of inflammatory mediators released by PBMCs treated with 50 µg/mL of G, MoS_2, or WS_2 for 24 h performed by Luminex assay. As positive control, cells were exposed to ConA (10 µg/mL) and LPS (2 µg/mL). Association clusters for samples are represented by dendrograms at the top of the heat map. Heatmaps (left panel) represents the z-score of the Log_2 concentration for each cytokine. The right panels display the Log_2 Fold Change of each experimental conditions as compared to negative controls (Ctrl) and the corresponding negative $Log_{10}p$ values corrected for multiple tests (Benjamini and Hochberg false discovery rate, FDR), computed using ANOVA contrasts. The red bar represents the *p* value cut-off (FDR < 0.05); z-score range for color coding was set between +2 and −2 (blue = down-regulated cytokines, negative z-score; red = up-regulated cytokines, positive z-score). Three independent samples were analyzed for each sample group.

response may be due to the different cell models and to the biocompatibility of our water-based formulations of 2D materials.

Next-generation sequencing of PBMCs exposed to TMDs

To investigate the molecular mechanism underlying the observed immune modulation exerted by the 2D materials, we evaluated their effect on genome-wide expression changes by next-generation sequencing (RNA-seq). To this end, PBMCs were exposed to 50 µg/mL of G, MoS_2, or WS_2 for 24 h or left untreated, and RNA was subjected to 3' mRNA sequencing following a sensitive and unbiased approach (Fig. 4 **and S5**). We performed principal component analysis on all analyzed transcripts (N = 19,959). We found that G- and TMD-treated samples clustered near the controls but separately from ConA- and LPS-treated samples, indicating that the investigated materials resulted in minimal perturbations of gene expression (Fig. 4**a**). Even with permissive corrected *p*-value (FDR) cutoffs, we did not observe genome-wide changes induced by TMDs. Thus, all 2D materials induced modest modulation in human PBMCs, affecting the expression of fewer genes than the positive controls, ConA and LPS. In particular, even if all the

materials displayed similar, modest effects on gene expression, WS_2 triggered the lowest number of differentially expressed genes. The expression of 483, 451, and 184 genes were modulated by G, MoS_2, and WS_2, respectively, whereas the positive controls ConA and LPS modulated the expression of 5497 and 1406 genes, respectively (FDR <0.05) (Fig. 4**b**). For functional predictions, we first used Venn diagrams to identify genes whose expression regulation was specific to one of the three 2D materials, as well as genes whose expression regulation was observed in two or three conditions. We found 289, 343, and 100 genes that were up-regulated by G, MoS_2, and WS_2, respectively. Down-regulated genes were analyzed similarly, revealing 194, 108, and 84 genes specifically repressed by G, MoS_2, and WS_2, respectively (Fig. 4**c**). List of all differentially expressed genes (FDR < 0.05) was used to plot a heatmap. It is notable that the ConA-treated samples clustered separately in the heatmap, suggesting a distinct response, while LPS- and G-exposed samples were clustered together. MoS_2 and WS_2 samples, on the other hand, were found to be clustered together with the untreated control samples, confirming that these materials induce minimal changes in the gene expression (Fig. 4**d**). Furthermore, pathway-enrichment analyses on differentially expressed genes (FDR < 0.05)
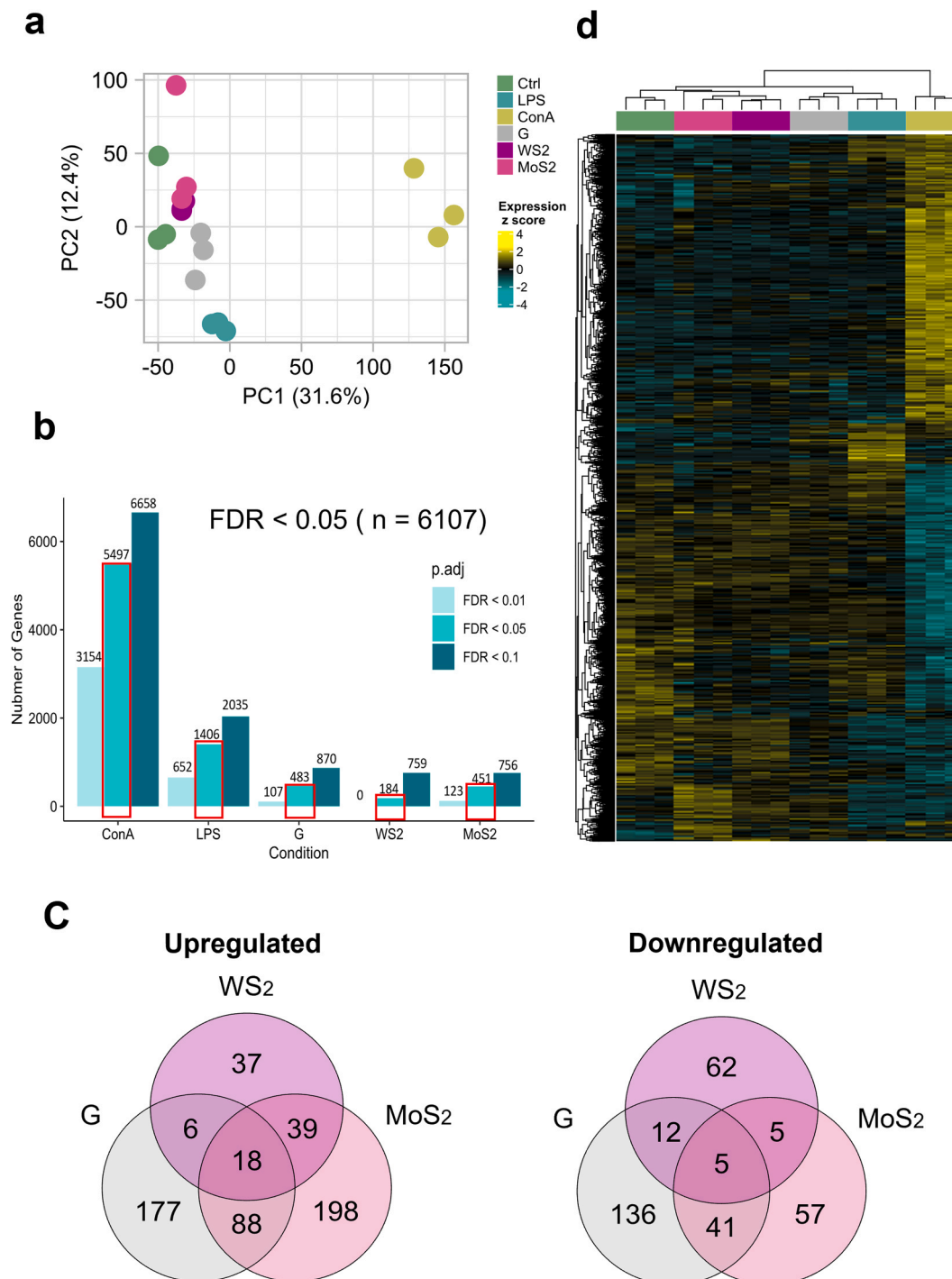
Fig. 4. Gene expression by m-RNA seq on human peripheral blood mononuclear cells (PBMCs). PBMCs were treated with 50 µg/mL of G, MoS_2, or WS_2 for 24 h. **a)** Principal component analysis based on the PBMC full normalized RNA-seq gene expression matrix. **b)** Numbers of differentially expressed genes based on different cutoffs of p-adjusted FDR value between experimental conditions and control. **c)** Venn Diagram of differentially expressed genes using FDR < 0.05. **d)** Gene expression analysis by mRNA-Seq. Heatmap of all differentially expressed genes between ConA, LPS, G, MoS_2, or WS_2 vs. control using FDR < 0.05.

showed that G induced more pronounced immune perturbations as compared to MoS_2 and WS_2 (Fig. S5). In particular, the overall immunological effect of WS_2 was negligible, consistent with the multiplex cytokine profiling data. Conversely, MoS_2 induced the activation of pathways implying monocyte-myeloid activation such as pathogen-induced cytokine storm (top-upregulated pathway), phagosome formation, granulocyte adhesion and diapedesis, and leukocyte extravasation signaling. Another central myeloid pathway activated by MoS_2 was TREM-1 (Triggering receptor expressed on myeloid cells-1). TREM-1 is a

positive regulator of CXCL8 (IL8) production [49]. This is consistent with what was observed by cytokine profiling, which demonstrated increased secretion of CXCL8 in MoS_2-treated PBMC (Fig. 3).

Overall, the gene-level effect of TMD analysis using RNA sequencing is coherent with the observed cytokine profiling. In detail, while G-exposed samples induced an effect comparable to that of the positive controls at the protein and molecular levels, MoS_2 and WS_2 exerted a limited impact in both analyses, significantly modulating only a few inflammatory mediators and pathways. In particular, among the

pathways mainly affected by MoS_2 we observed the TREM1 signaling that amplifies TLR-induced inflammation, the complement system, and the differential regulation of cytokine production in macrophages and T helper cells. These findings are in line with the MoS_2-induced inhibition of inflammatory mediators (CXCL10, CCL22, and CCL11) consistent with a suppression of the innate-adaptive immune response crosstalk. In addition, MoS_2 had a significant impact on the genes involved in the inflammasome pathway, in line with the upregulation of monocyte/myeloid activators observed in the analysis of inflammatory mediators modulated by this material, in particular of monocyte/myeloid chemoattractant protein CCL2, MI, CXCL8, and CXCL1 as well as IFNγ, a primary activator of macrophages.

TMD modulation of Mo-dependent enzymes

Unlike tungsten (W), molybdenum (Mo) is a bioavailable element, constituting the active sites of four mammalian enzymes that utilize Mo as a cofactor (Moco) [50]. Therefore, to better understand the mechanisms underlying the biological interactions of MoS_2, it is important to evaluate its potential biotransformation that could provide cofactors for these enzymes. In fact, this could lead to increased activity of sulfite oxidase, mitochondrial amidoxime-reducing component, aldehyde oxidase, and xanthine oxidoreductase, with consequences on a diversity of biological processes require redox reactions dependent on these enzymes such as cell stress response and mitochondrial respiration.

Recently, it has been reported that the biotransformation of MoS_2-based nanodots leads to the incorporation of Mo into Mo-dependent enzymes [51]. We recently reported the bioavailability of MoS_2 following the uptake of the 2D nanosheets in macrophages as proven by the upregulation of genes encoding Mo-dependent enzymes and genes involved in the Moco biosynthetic pathway [12].

The bioavailability of Mo in macrophages triggered the Moco biosynthetic pathway with the upregulation of *MOCS1*, *MOCS3*, and *GPHN* genes [12]. Furthermore, MoS_2 significantly induced the expression of the four mammalian Mo-dependent enzymes *AOX1*, *XDH*, *SUOX*, and *MARC1*, confirming the Mo bioavailability upon uptake of MoS_2 in macrophages [12]. On the other hand, in cells treated with WS_2, no changes were observed in genes involved in the Moco pathway, thus confirming that the modulation of the pathway was specific for Mo [12].

In PBMCs, however, the effect of MoS_2 on genes involved in Moco biosynthetic pathway and genes encoding Mo-dependent enzymes appeared to be less evident and specific than what was observed in macrophages. In fact, only a non-statistically significant increase of *MOCS3* (Moco biosynthetic pathway) and *SUOX* a (Mo-dependent enzymes) was observed after incubation with MoS_2, which was however also observed after WS_2 (Fig. S6).

Label-free detection of TMDs in sixteen human primary immune cell types

A critical aspect of expanding the biomedical applications of nanomaterials is their detection in cells and tissues. Therefore, having established the biocompatibility of the investigated TMDs, we evaluated their possible label-free detection by exploiting high-dimensional technologies. To this end, we explored the potential detection of MoS_2 and WS_2 using CyTOF while dissecting their immunological effects on individual cells through this high-dimensional technology. The specific atomic masses of the 2D materials selected in this work enabled mass cytometry detection of MoS_2 and WS_2 in the molybdenum (^{95}Mo) and tungsten ($^{180-186}W$) channels, respectively. We included G as a control, as this carbon-based material cannot be detected by CyTOF. PBMCs were exposed to 50 μg/mL of MoS_2 or WS_2 for 24 h. Sixteen distinct immune cell subpopulations were identified according to the expression profile of several clusters of differentiation (CD) markers on the surface of immune cells (Fig. S7 **and** table S2). The two TMDs were compatible with the commercial (metal-tagged) antibody panels used for the immune-phenotyping and immune functionality evaluation. We chose

the intermediate sub-cytotoxic concentration of 50 μg/mL and the 24 h time-point based on the results obtained by flow cytometry (Fig. 2**b-d and** Fig. S4a **and** b) and to avoid the saturation of molybdenum and tungsten intensity while still ensuring noticeable changes in cellular signaling, according to our previous experience with 2D materials belonging to the graphene family [27,33,34]. We performed computational tSNE analysis as previously described [27,33]. The tSNE plots (Fig. 5**a and S8**), heat maps (Fig. 5**b and c**), and bar graphs (Fig. 5**d-f**) describe that both TMDs were naturally visible at the single-cell level and interacted with a wide number of immune cell subpopulations as indicated by the percentage of TMD positive cells (Fig. 5**f**). Of the two materials, WS_2 had the strongest signal and showed extensive interaction with all the PBMC subsets identified (Fig. 5**c, e, and f**). In particular, monocytes (classical and non-classical), DCs (monocytoid and plasmacytoid), and B cells (naïve, memory, and plasma B cells) showed the most prominent interactions with WS_2. Similarly, these subpopulations were the central immune subsets able to interact with MoS_2, albeit to a lesser extent (Fig. 5**b, d, and f**). Moreover, the single-cell analysis by cisplatin staining showed no signs of cell death induced by materials, demonstrating high biocompatibility of MoS_2 and WS_2 towards all the 16 cell subpopulations analyzed, regardless of the extent of interaction (Fig. S9 and S10). In addition, to support the cellular interaction data of CyTOF, we evaluated TMD interaction and detection by IMC on PBMCs after exposure to 50 μg/mL of MoS_2 or WS_2 for 24 h (Fig. 5**g**). The materials were successfully identified by IMC, and their signals were mutually exclusive with that of DNA, thus indicating that they did not localize to the cell nucleus. Similar to the CyTOF analysis, WS_2 showed a higher signal intensity than MoS_2 (Fig. 5**g**).

In vivo label-free detection of TMDs in intact tissues and in all immune cell subsets

Finally, we examined whether high-dimensional technologies could also be applied to study TMDs in vivo. To this end, mice were exposed to a mixture of the two TMDs, and the single-cell and tissue levels were studied using CyTOF and MIBI-TOF techniques (Fig. 6**a**, Table S3 and S4). We intravenously (i.v.) injected C57BL/6 J male mice with 20 mg/kg of a mixture of the TMDs (MoS_2 and WS_2) (Figs. 6, 7, **and S11**). Both materials were easily detectable by multiple single-cell staining and at the tissue level. At 24 h post-intravenous injection, MoS_2 and WS_2 were still detectable in the liver, lung, spleen, and blood (Fig. 6**b-d**). In particular, the liver displayed the highest TMD levels expressed as ^{95}Mo and $^{180-186}W$ signal intensity, followed by the lung, spleen, and blood (Fig. 6**b**). According to the signal intensity deconvolution for each material, between the two TMDs, WS_2 showed the highest signal intensity in all organs analyzed (Fig. 6**c**). As revealed by the TMD mean intensity (MI) detected in the different immune cell populations analyzed per organ, the materials were detectable in all cell subsets analyzed, mainly in cell types with phagocytic activity $CD11b^+$ $CD11c^+$ and $CD11c^+$ DCs, monocytes (classical and non-classical), and neutrophils (Fig. 6**d**). Grouped bar plots show the TMD MI for all immune cell subpopulations identified per organ (Fig. 6**e**).

Additionally, we conducted MIBI-TOF analysis on mouse organs to determine whether TMDs could be detected in situ in intact tissues. Following our previously reported protocols for tissue preparation [25], we stained the tissues with nine metal-labeled antibodies and visualized them using MIBI-TOF. As shown in Fig. 7, MoS_2 and WS_2 signals were detected in all the main organs in the molybdenum (^{95}Mo) and tungsten ($^{180-186}W$) channels, respectively, together with the expected antibody signals. No signs of tissue damage were reported. In the tungsten channel, the signal was brighter, demonstrating greater sensitivity to material detection. TMDs were detected mainly in the liver and lungs, followed by the spleen (Fig. 7).

Our results align with a recent study demonstrating that MoS_2 nanodots complexed with albumin were visible in the same organs by inductively coupled plasma mass spectrometry after 24 h [51].
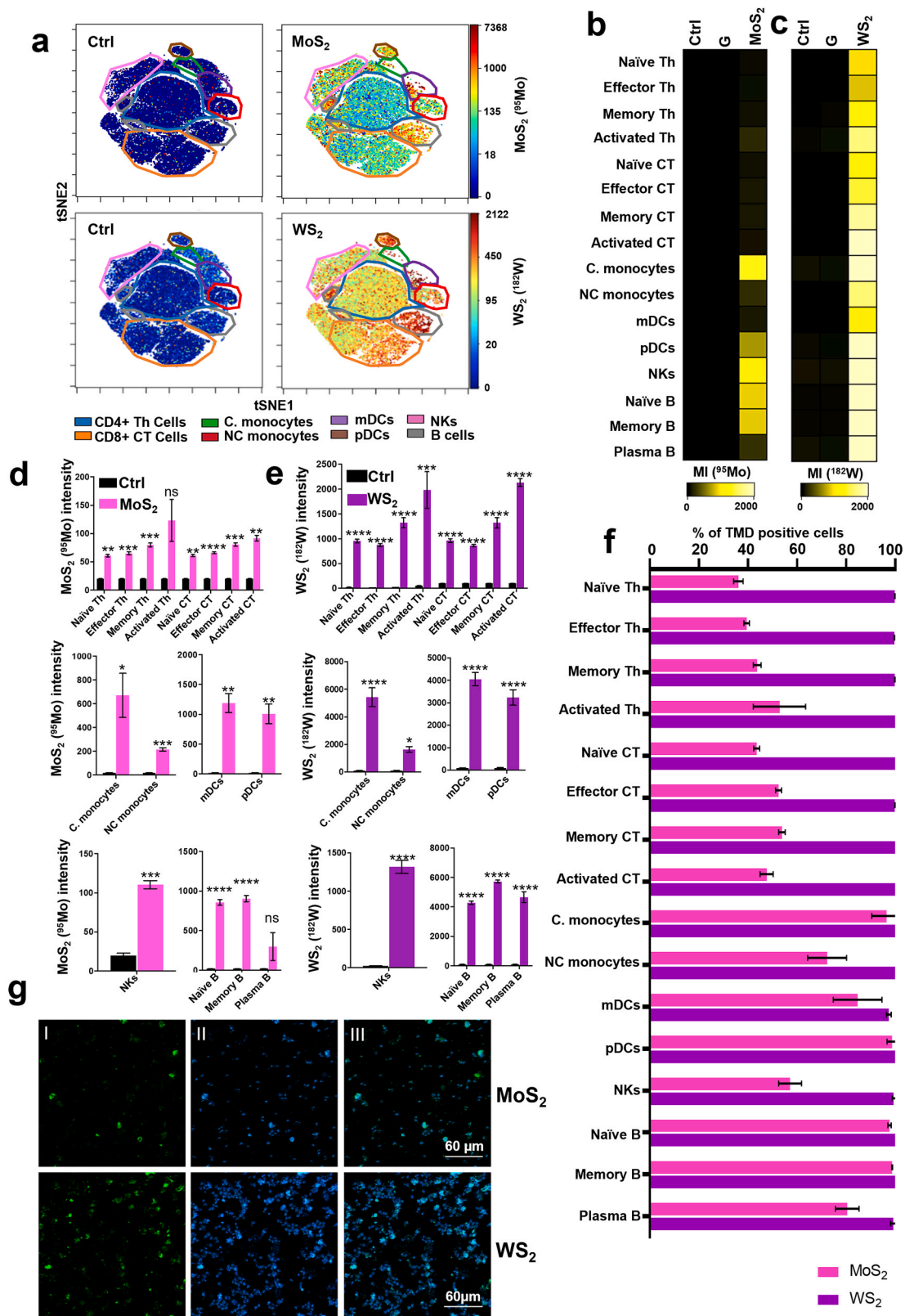
Fig. 5. TDMs cell interaction at single-cell level on human PBMCs. PBMCs were treated with 50 µg/mL of WS$_2$ or MoS$_2$ and analysed at CyTOF. **a)** t-SNE plots showing MoS$_2$ and WS$_2$ mean intensity in treated and untreated immune subpopulations. **b-c)** Representative heat map reporting MoS$_2$ and WS$_2$ mean intensity in all subpopulations identified. **d)** Graph representing the uptake of MoS$_2$ and **e)** WS$_2$ expressed as median for each specific channel (^{95}Mo and ^{182}W) in all the major immune subpopulations identified. All the experiments were performed in triplicate and shown as means±SD. Statistical differences: *$p < 0.05$; **$p < 0.01$; ***$p < 0.001$, ****$p < 0.0001$ (One-way ANOVA followed by Tukey's multiple comparison test). **f)** Histogram showing WS$_2$ or MoS$_2$ median intensity and % of positive cells in all PBMC subpopulations identified. **g)** 2D material detection by imaging mass cytometry (IMC) of human PBMCs. IMC images (I panels) reporting in green the single-cell detection of WS$_2$ or MoS$_2$. IMC images (II panels) reporting in blue and light blue the DNA signal. IMC images (III panels) reporting a composite image of DNA (blue) and WS$_2$ or MoS$_2$ (green).
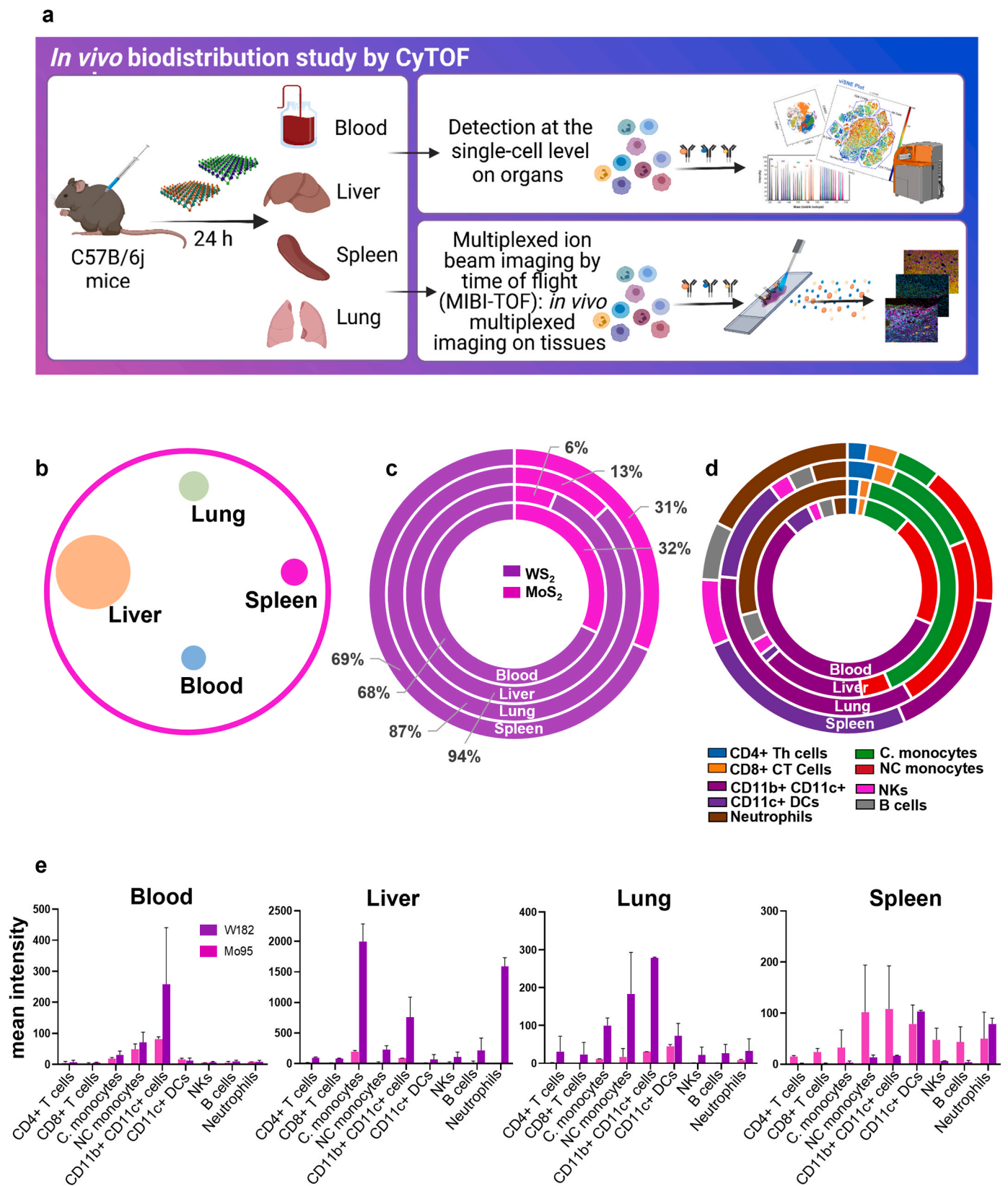
Fig. 6. Single-cell biodistribution analysis of TMDs in vivo. C57B/6j male mice (n = 3) were injected I.V. with 20 mg/kg of TMDs or left untreated. After 24 h mice were sacrificed and blood, liver, lungs, and spleen were harvested and stained for mass cytometry analysis. **a)** Workflow of the experiment. **b)** Representative circle chart reporting the total TMD signal intensity detected per organ. **c)** Signal intensity deconvolution for each TMD in all the organs analyzed. **d)** Total TMD intensity detected per immune cell population in each analyzed organ. **b-d)** Report the average data among the biological replicates (n = 3). **e)** Deconvoluted TMD mean intensity subtracted to control in all immune subpopulations identified per organ reported as grouped bar plots. Data are presented as mean ± SEM among the replicates.
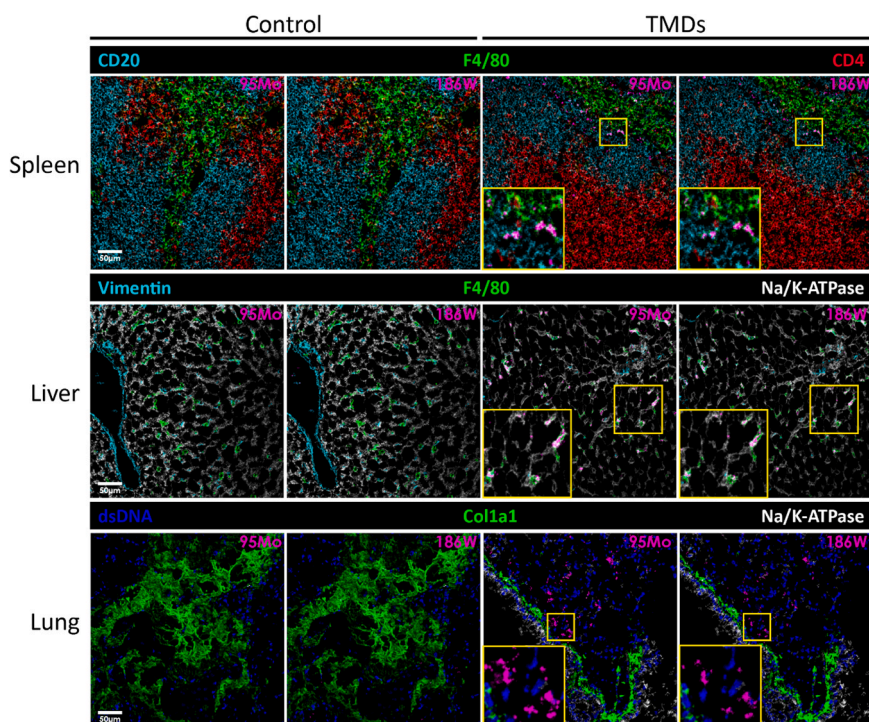
Fig. 7. In vivo biodistribution of TMDs in tissues. MIBI-TOF imaging of tissues from control and TMDs-injected mice stained with the indicated metal-labeled antibodies. TMD signal (purple) was detectable across all tissues in the molybdenum (^{95}Mo) and tungsten (^{186}W) channels. Scale bar- 50 µm.

However, unlike the latter study, in which a tissue-destructive method was used to monitor the levels of molybdenum [49], our approach (using cell suspensions and intact tissues) allowed for the detection of molybdenum and tungsten at the single-cell level in multiple cell types and in situ in intact tissues.

Conclusions

The results obtained in this work demonstrate excellent biocompatibility of water-based and defect-free MoS_2 and WS_2, prepared by liquid-phase exfoliation via non-covalent functionalization with 1-pyrenesulfonic acid sodium salt. It is important to note that this study has addressed the nano-bio interactions of nanomaterials using 16 primary human immune cells (not transformed cell lines). Indeed, the human immune system remains our most important model for the study of human health and diseases [52]. Our functional analysis at the protein and gene level revealed that MoS_2 and WS_2 had a limited effect on immune cell functionality as compared to graphene, the most explored 2D material for biomedical applications, to date. In particular, among the two TMDs, WS_2 had the lowest impact on inflammatory mediators and differentially expressed genes in PBMCs. Furthermore, our in-depth ex vivo study at the single-cell level qualifies MoS_2 and WS_2 as bio- and immunocompatible on all the sixteen primary immune cell subpopulations analyzed. Moreover, we presented evidence that their mass enables their label-free detection by mass cytometry-based technologies (CyTOF and IMC) and multiplexed ion beam imaging (MIBI-TOF). The materials were found to interact with specific immune cell subpopulations, particularly with monocytes, DCs, and B cells. Among the two TMDs, WS_2 exhibited greater brightness and signal intensity in all the cell subpopulations and tissues analyzed using ex vivo and in vivo models. In addition, the materials were highly compatible and non-overlapping with the currently available mass cytometry panels, including 48 metal-tagged antibodies and palladium-based barcoding used for CyTOF analysis. Moreover, we used the molybdenum (^{95}Mo) and tungsten ($^{180-186}$W) channels, not yet explored for commercial mass cytometry tags. The present study represents a breakthrough in terms of

the non-destructive and label-free detection of TMDs in a complex pool of immune cells as well as in situ in tissues from exposed animals.

Overall, our findings provide a fundamental understanding of the biological profile of MoS_2 and WS_2, thus proposing a versatile high-dimensional strategy to investigate TMD-based nanoplatforms for their future applications in biomedicine.

Materials and methods

2D material preparation and characterization

Aqueous 2D crystal dispersions were prepared via liquid-phase exfoliation in water, following the methodology developed in previous publications [30,37,53]. Briefly, graphite flakes were provided by Graphexel ltd, while bulk molybdenum (IV) sulfide powder (MoS_2, 2 µm, 99.0 %), bulk tungsten (IV) sulfide powder (WS_2, 2 µm, 99.0 %), and 1-pyrenesulfonic acid sodium salt (PS1) ($\geq$97.0 %), were purchased from Sigma-Aldrich. For the preparation of the dispersions, 300 mg of each powder was added to 100 mL of de-ionized (DI) water, in which 50 mg of PS1 was previously dissolved. The mixture was then sonicated at 600 W for 7 days using a Hilsonic bath sonicator. Subsequently, un-exfoliated bulk material was removed by centrifuging the solution (Sigma 1–14k refrigerated centrifuge) at 3500 rpm (903 g) for 20 min, and then the supernatant, containing well-dispersed nanosheets in water, was collected. The excess pyrene molecules were removed by 2-step centrifugation (Sigma 1–14k refrigerated centrifuge) at 15, 000 rpm (16,600 g) for 60 min. After each centrifugation step, the supernatant was removed, and the sediment was redispersed in DI water. To increase the concentration, a smaller volume of DI water was added to the sediment after the last centrifugation.

The final concentration of nanosheets in the dispersion was determined using UV-Vis spectroscopy. The Beer-Lambert law was used to derive the concentration by assuming an absorption coefficient of 2460 L•g^{-1}•m^{-1} at 660 nm, 3400 L•g^{-1}•m^{-1} at 672 nm, and 2756 L•g^{-1}•m^{-1} at 629 nm for graphene, MoS_2, and WS_2, respectively [38,54–57]. A Perkin-Elmer l-900 UV-Vis-NIR spectrophotometer was used to

acquire the spectra.

Raman measurements were performed using a Renishaw Invia Raman spectrometer equipped with a 514.5 nm excitation line and 2.0 mW laser power. Diluted 2D crystal dispersions were dropcast onto silicon substrates, and measurements were performed on isolated and individual flakes. The Raman spectra were taken with a 100X NA0.85 objective lens and 2400 grooves/mm grating. The exfoliated 2D crystals showed characteristic peaks for each 2D crystal (Fig. S1b-**d**), demonstrating that no degradation of the 2D crystals occurred during sonication. We remark that Raman spectroscopy cannot provide quantitative thickness analysis on solution-processed graphene and TMDs.

The statistical lateral size and height distribution of the exfoliated nanosheets were measured using Atomic Force Microscopy (AFM). A Bruker Atomic Force Microscope (MultiMode 8) in Peak Force Tapping mode, equipped with ScanAsyst-Air tips, was used. The sample was prepared by drop casting the solution on a clean silicon substrate; several areas of 100 μm^2 were scanned, and about 200 flakes were selected for lateral size analysis. Lateral dimension and thickness distributions of graphene nanosheets were carried out using Gwyddion scanning probe microscopy data processing software. Fig. S1h shows the average size and thickness for each 2D material. The relation between the size and thickness of the nanosheets is shown in Fig. S1e-**g**. We remark that the thickness measured by the AFM takes into account the adsorbed stabilizer, which cannot be removed completely by simple washing. Hence, the number of layers cannot be directly derived by the measured thickness, and a comparison of thickness values between 2D materials, which have been produced by using different methods, can be misleading. Electron microscopy analysis shown in previous works [30] has demonstrated that LPE assisted by PS1 gives rise to high crystalline and well-exfoliate flakes.

Human monocyte-derived macrophages isolation and culture

Peripheral blood mononuclear cells (PBMCs) were isolated from buffy coats obtained from healthy human blood donors (Karolinska University Hospital, Stockholm, Sweden) by density gradient centrifugation using Lymphoprep™, as described previously [58]. Then, PBMCs were positively selected for CD14 expression using CD14 MicroBeads (Miltenyi Biotech Ltd). To obtain human monocyte-derived macrophages (HMDMs), CD14+ monocytes were cultured in RPMI-1640 cell medium supplemented with 2 mM L-glutamine, 100 IU/mL penicillin, 100 μg/mL streptomycin, and 10 % heat-inactivated FBS, supplemented with 50 ng/mL recombinant M-CSF (R&D Systems) for three days.

Cell viability assay

Cells were seeded in 96-well plates RPMI-1640 cell medium at a density of 6×10^4 cells/well and exposed to nanomaterials for 24 h at the indicated concentrations or were maintained in cell medium alone (negative control) at 37 °C in a humidified 5 % CO_2 incubator. Lactate dehydrogenase (LDH) release assay was performed for cytotoxicity assessment using the CytoTox 96® nonradioactive cytotoxicity kit (Promega). After exposure, 50 μL of culture supernatant were removed from the cells and loaded onto a 96-well plate. For the measurement of intracellular LDH, the cells were exposed to lysis buffer at 37 °C for 30 min. Then, 50 μL of the lysis were transferred to a 96-well plate, and 50 μL of the reaction substrate were added to each sample. The formation of red formazan was read at 492 nm using a spectrophotometer (Tecan Infinite F200 plate reader, Männendorf, Switzerland). The percentage of cell viability was calculated based on the ratio between the absorbance of each sample compared with the negative control. The experiments were performed with at least three individual donors and three technical replicates for each concentration of each 2D material. Results were expressed as percentage cell viability versus maximum LDH release. To control for possible assay interference, the TMDs were maintained in a cell-free medium and mixed with the reaction substrate reagent; no interference was observed (data not shown).

TET assay for endotoxin

Graphene, MoS_2, and WS_2 were assessed for endotoxin content using the TNF-α expression test (TET), which enables unequivocal detection of endotoxin with a sensitivity comparable to that of the conventional LAL assay, but without any interference with the assay [39]. In brief, human monocyte-derived macrophages (HMDM), obtained as described above, were exposed to a non-toxic dose of TMDs (25 μg/mL) or to 0.1 μg/mL LPS (Sigma-Aldrich) in the presence or absence of the LPS inhibitor, polymyxin B (10 mM) (Sigma-Aldrich), and TNF-α secretion was measured at 24 h with the Human TNF-α ELISA Kit purchased from MABTECH (Sweden).

Interleukin-1β ELISA

HMDMs were primed or not with LPS (0.1 μg/mL) for 2 h and then exposed to G, MoS_2, or WS_2 (25 μg/mL) for 24 h. The exposed cell media were collected and stored at −80 °C for further analysis. The IL-1β release was determined by using a human IL-1β ELISA kit (Invitrogen, Sweden). Absorbance was measured at 450 nm using a Tecan Infinite F200 plate reader. Results are expressed as pg/60.000 cells of released cytokine, based on at least three independent experiments using cells from different blood donors. To assess the role of caspases and NLRP3 [59], cells were incubated for 1 h with or zVAD-FMK (20×10^{-6} M) (Sigma) or MCC950 (10×10^{-6} M) (Sigma), respectively, and subsequently exposed to 25 μg/mL of G, MoS_2 or WS_2 for 24 h in RPMI-1640 cell culture medium supplemented with 10 % FBS. The exposed cell media were collected, and IL-1β quantification was done using ELISA as described above.

Human monocyte-derived macrophages uptake by TEM

For Transmission Electron Microscopy (TEM) analysis, HMDMs were exposed to G, MoS_2, or WS_2 for 24 h at a concentration of 25 μg/mL. After exposure, the cells were fixed in 2.5 % glutaraldehyde in 0.1 M phosphate buffer, pH 7.4 at room temperature for 30 min and further fixed overnight in the refrigerator. Samples were rinsed in 0.1 M phosphate buffer and centrifuged. The pellets were then post-fixed in 2 % osmium tetroxide in 0.1 M phosphate buffer, pH 7.4 at 4 °C for 2 h, dehydrated in ethanol followed by acetone, and embedded in LX-112. Ultrathin sections (approx. 50–60 nm) were cut by using a Leica ultracut UCT/Leica EM UC 6. Sections were contrasted with uranyl acetate followed by lead citrate and examined using a Tecnai 12 Spirit Bio TWIN transmission electron microscope (FEI Company) at 100 kV/Hitachi HT 7700. Digital images were taken using a Veleta camera (Olympus Soft Imaging Solutions).

PBMC isolation and culture

PBMCs were harvested from ethylenediamine tetraacetic acid (EDTA)-venous blood from informed healthy donors (25–50 years old) using a Ficoll-Paque (GE Healthcare, CA, USA) standard separation protocol. Informed signed consent was obtained from all the donors. Cell separation and experiments were performed immediately after blood drawing. PBMCs were cultured in 24-well plates in RPMI 1640 medium (Life Technologies), supplemented with 1 % penicillin/streptomycin (Life Technologies), and 10 % heat-inactivated fetal bovine serum (Life Technologies). At least 1×10^6 cells/sample in each experiment were used. Experiments were carried out using at least three healthy donors, each in technical triplicate.

PBMC uptake by TEM

For Transmission Electron Microscopy (TEM) analysis, samples were fixed with 2.5 % glutaraldehyde in 0.1 M sodium cacodylate buffer pH 7.4 ON at 4 °C. The samples were postfixed with 1 % osmium tetroxide plus potassium ferrocyanide 1 % in 0.1 M sodium cacodylate buffer for 1 h at 4 °C. After three water washes, samples were dehydrated in a graded ethanol series and embedded in an epoxy resin (Sigma-Aldrich).

Ultrathin sections (60–70 nm) were obtained with an Ultrotome V (LKB) ultramicrotome, counterstained with uranyl acetate and lead citrate, and viewed with a Tecnai G^2 (FEI) transmission electron microscope operating at 100 kV. Images were captured with a Veleta (Olympus Soft Imaging System) digital camera.

Cytotoxicity by flow cytometry

To evaluate the cytotoxicity of G, MoS$_2$, and WS$_2$, PBMCs were incubated for 24 h at 37 °C as described above with increasing doses of each nanomaterial (i.e., 25, 50, and 100 μg/mL). Ethanol at 70 % was used as a positive control, while samples incubated with medium alone were used as negative controls. Cell death was analyzed by means of Zombie Aqua staining (BioLegend).

Cells were processed by flow cytometry (FACS Canto II, BD Bioscience, CA, USA), and data were analyzed by FlowJo™ Software[12] as previously reported [13–15].

Calcein AM/ethidium homodimer-1 assay

PBMCs were treated for 24 h with different concentrations of (25, 50, and 100 μg/mL) of G, MoS$_2$, and WS$_2$, and calcein AM/ethidium homodimer-1 staining was performed by incubating cells with 2 μmol/L calcein AM and 5 μmol/L ethidium homodimer (Live/Dead® Viability/Cytotoxicity kit, Invitrogen) for 45 min at 37 °C in the dark. Ethanol 70 % was used as a positive control, while samples incubated with medium alone were used as negative controls. The assay discriminates live from dead cells by simultaneously staining with green-fluorescent calcein-AM (excitation wavelength of 485 nm and emission wavelength of 530 nm) to indicate intracellular esterase activity and red-fluorescent ethidium homodimer-1 (excitation wavelength of 530 nm and emission wavelength of 645 nm) to indicate loss of plasma membrane integrity. Plasma membrane integrity and esterase activity were measured by a Fluorescence Microplate Reader (TECAN infinite M200PRO, Switzerland).

Luminex® multi-plex arrays

To evaluate the impact of TMDs on cytokine release by PBMCs, cells were incubated for 24 h with 50 μg/mL of the materials. LPS (2 μg/mL; Sigma – Aldrich, Missouri, USA) was used as a positive control, while samples incubated with medium alone were used as negative controls. Supernatants were collected and analyzed by Luminex technology using Bio-Plex Pro Human Chemokine 40-plex Panel (Bio-Rad) to measure C-C Motif Chemokine Ligand (CCL) 21 (CCL21), chemokine (C-X-C motif) ligand (CXCL) 13 (CXCL13), CCL27, CXCL5, CCL11, CCL24, CCL26, C-X3-C Motif Chemokine Ligand 1 (CX3CL1), CXCL6, granulocyte macrophage-colony stimulating factor (GM-CSF), CXCL1, CXCL2, CCL1, interferon gamma (IFN-γ), interleukin (IL)-1β, IL-2, IL-4, IL-6, CXCL8, IL-10, IL-16, CXCL10, CXCL11, CCL2, CCL8, CCL7, CCL13, CCL22, macrophage migration inhibitory factor (MIF), CXCL9, CCL3, CCL15, CCL20, CCL19, CCL23, CXCL16, CXCL12, CCL17, CCL25 and tumor necrosis factor (TNF)-α. 5-parameter-Logistic regressions with a power low variance weighing were calculated for each cytokine standard with a recovery range of 70–130 % using Bioplex Manager V6.2 (BioRad). Concentration falling within the recovery range, expressed in pg/mL was extrapolated from the median fluorescence intensity of each cytokine bead set. For analytes above or below the standard recovery ranges, upper and lower limits of quantification computed from the standard curves were substituted. Data were then Log2 transformed and compared across experiments by fitting a general ANOVA model with contrast between groups; *p* values were corrected using Benjamini and Hochberg false discovery rate, FDR; statistically significant *p*-value cutoff was set at FDR $p < 0.05$. Values out of range, "00R>" or "00R<", were replaced, respectively, with the maximum or minimum value for the analyte across samples, indicated with (*), or, when not possible, with the upper (ULOQ) or lower limit of quantification (LLOQ) for that analyte, respectively.

RNA sequencing

RNA extraction and QC

To evaluate the impact of TMDs on PBMCs, cells were incubated with 50 μg/mL of MoS$_2$ or WS$_2$ for 24 h. LPS (2 μg/mL; Sigma – Aldrich, Missouri, USA) and Concanavalin A (ConA, 10 μg/mL; Sigma – Aldrich, Missouri, USA) were used as positive controls, while samples incubated with medium alone were used as negative controls. After treatment, the cell suspension was transferred from each well into RNase-free 1.5 mL tubes, and cells were washed two times with 1 mL of PBS. Cells were then resuspended in 350 μL of RLT Buffer freshly additionated with 1 % β-mercaptoethanol and stored at −80 °C.

RNA was extracted using the RNAeasy Kit (Qiagen. The methodology has been followed detail in kit instruction). RNA was quantitated on a NanoDrop™ (ThermoFisher) and QCed using an Agilent 2100 Bioanalyzer (Agilent, Santa Clara, California, USA). All samples had a RIN > 7.5.

Normalization and statistical analysis

mRNA-sequencing was performed using QuantSeq 3' mRNA-Seq Library Prep Kit FWD for Illumina (75 single-end) with a read depth of average 8.35 M, and average read alignment of 80.95 %. Single samples were sequenced across four lanes, and the resulting FASTQ files were merged by sample. All FASTQ passed QC and were aligned to the reference genome GRChg38/hg19 using STAR 2.7.9a. BAM files were converted to a raw counts expression matrix using HTSeq-count. Then "betweenLaneNormalization" normalized data (EDAseq) was quantiled normalization and log2 transformed (total transcript mapped to genes = 19,959 genes). All downstream analysis was performed using RStudio (Version 4.1., RStudio Inc.). Global transcriptional differences between samples were assessed by principal component analysis using the "prcomp" function. Differential gene expression analysis between conditions and untreated was performed using Limma via Bioconductor package "limma v. 3.52.2" [PMID 25605792] with Benjamini-Hochberg (B-H) FDR. In each comparison, genes with rows sum equal to zero were removed. To illustrate the differentially expressed genes overlap between the conditions, R CRAN package "VennDiagram v. 1.7.3" was used. Differentially expressed genes were then plotted in a heatmap using Bioconductor package "ComplexHeatmap v. 2.12.0". For enriched pathway analysis, list of differentially expressed genes (FDR < 0.05) was uploaded to Ingenuity Pathway Analysis (IPA). Pathways data were exported from IPA as excel file and used to regenerate the figure using R CRAN package "ggplot2 v. 3.3.6". Histogram were plotted using R CRAN package "ggplot2 v. 3.3.6".

Single-cell mass cytometry analysis

Single-cell mass cytometry analysis was carried out using isolated PBMCs, obtained as previously reported. PBMCs were cultured in 6-well plates at a concentration of 4×10^6 cells per well and treated with 50 μg/mL of G, MoS$_2$, or WS$_2$ for 24 h at 37 °C. LPS (0.5 μg/mL; Sigma – Aldrich, Missouri, USA), ethanol for cell biology (EtOH 70 %), and untreated cells were used, respectively, as positive and negative controls.

Cells were incubated with Brefeldin A (Invitrogen, CA, USA) to a final concentration of 10 μg/mL, 6 h before the end of the treatment. After the incubation time, cells were washed with a sterile solution of phosphate-buffered saline (PBS), EDTA 0.5 M, and 5 % of fetal calf serum (FCS).

Cells were then combined using Cell-ID 20-Plex Pd Barcoding Kit (Fluidigm, CA, USA). The barcoded sample was stained with Cell-ID Cisplatin (Fluidigm, CA, USA) 1:1000, Maxpar Human Peripheral Blood Phenotyping Panel Kit (Fluidigm, CA, USA) following the manufacturer staining protocols.

In synthesis, in order to guarantee a uniform cell labeling with the palladium barcode, cells were fixed and permeabilized by means of 1X Fix I Buffer and 1X Barcode Perm Buffer.

After the barcoding step, samples were pooled together and resuspended in Maxpar Cell Staining Buffer into a 5 mL polystyrene round-bottom tube.

The surface marker antibody cocktail (1:100 dilution for each antibody, final volume 800 μL) was added to the tube. The sample was mixed and incubated for 30 min at room temperature. After incubation, the sample was washed twice with Maxpar Cell Staining Buffer. Cells were then fixed by incubating the sample with 1 mL of 1.6 % paraformaldehyde for 10 min. At the end of the incubation, cells were washed twice with Maxpar Cell Staining Buffer and stained overnight with Cell-ID Intercalator-Ir solution at the final concentration of 125 nM. Prior to data acquisition, the samples were washed twice with Maxpar Cell Staining Buffer, resuspended with 2 mL of Maxpar water, and filtered using a 0.22 μm cell strainer cap to remove possible cell clusters or aggregates. Data were analyzed using mass cytometry platform CyTOF2 (Fluidigm Corporation, CA, USA).

Gating strategy and statistical analysis

The CyTOF data analysis was carried out accordingly to the methods described by Orecchioni M et al. [27] and Bendall et al. [60] Briefly, normalized, background subtracted FCS files were uploaded into Cytobank for analysis. The gating strategy excluded doublets, cell debris, and dead cells by means of Cell-ID Intercalator-Ir and LD. Specific PBMC subsets and subpopulations were assessed as reported in Fig. S7, in detail: T cells (CD45+ CD19- CD3+), T helper (CD45+ CD3+ CD4+), T cytotoxic (CD45+ CD3+ CD8+), T naive (CD45RA+ CD27+ CD38− HLADR−), T effector (CD45RA+ CD27− CD38− HLADR−), and activated (CD38+ HLADR+), B cells (CD45+ CD3- CD19+), B naive (HLADR+ CD27−), B memory (HLADR+ CD27+), plasma B (HLADR− CD38+), NK cells (CD45+ CD3− CD19− CD20− CD14− HLADR− CD38+ CD16+), Classical monocytes (CD45+ CD3− CD19− CD20− HLADR+ CD14+), Intermediate monocytes (CD45+ CD3− CD19− CD20− HLADR+ CD14dim CD16+) Non classical monocytes (CD45+ CD3− CD19− CD20− HLADR+ CD14- CD16+), mDC (CD45+ CD3− CD19− CD20− CD14− HLA− DR+ CD11c+ CD123−), and pDC (CD45+ CD3− CD19− CD20− CD14− HLADR+ CD11c− CD123+). The heat map visualization, realized with Cytobank, compared marker fluorescence of the treated populations with mean fluorescent intensity vs. the untreated control. viSNE tool was applied. viSNE, a cytometry analysis tool implemented in Cytobank, uses t-stochastic neighbor embedding (t-SNE) to show single cells in a two- or three-dimensional plot, according to their relationships. 9 cell surface markers were exploited in order to produce the viSNE map: CD3, CD4, CD8a, CD11c, CD14, CD16, CD19, CD20, CD123, and HLADR.

Cellular detection by IMC

Metal-labeled antibodies were provided by Fluidigm, from the standard CyTOF catalog (http://maxpar.fluidigm.com/product-catalog-metal.php). Metal-labeled antibody cocktails were prepared in 0.1 % Tween-20 % and 1 % BSA in PBS. All samples were first blocked with 1 % BSA and 0.2 mg/mL mouse IgG Fc fragment (Thermo Scientific) in PBS for 30 min and then incubated with antibody cocktail for 1.5 h at RT, followed by washing with PBS and staining with DNA intercalator Ir-191/193 (Fluidigm) and CD45 (HI30)−89Y (Fluidigm) for 30 min. Slides were again washed with PBS and rinsed with ddH₂0 for 5 s and dried overnight at room temperature prior to IMC analysis.

ROIs of 500 × 500 μm undergo laser ablation aerosolizing a 1 μm² area/pulse (200 Hz), followed by ionization and quantification in the CyTOF Helios instrument. Ion mass data is collected for each pulse and processed to render images for each individual channel at 1 μm resolution, where the intensity of each pixel corresponds to the ion count value. Raw data were analyzed using Fluidigm MCD viewer program.

In vivo biodistribution of TMDs

For the in vivo biodistribution experiments, three male C57BL/6J (cat.# 000664) mice per group were used. Mice were injected I.V. retro-orbitally with a 100 μL cocktail of TMDs (MoS₂ and WS₂), 20 mg/g each in sterile PBS) or only sterile PBS. After 24 h, mice were euthanized by CO₂ inhalation followed by blood withdrawal via cardiac puncture before further organ and tissue dissection. All experiments followed the guidelines of the La Jolla Institute for Immunology (LJI) Animal Care and Use Committee. Approval for the use of rodents was obtained from LJI according to criteria outlined in the Guide for the Care and Use of Laboratory Animals from the National Institutes of Health.

Blood, spleen, lungs, and liver were harvested, and single-cell suspensions were isolated by following procedures. Blood was withdrawn via cardiac puncture and collected in EDTA-coated tubes (Sarstedt). Erythrocytes were lysed using 1x RBC lysis buffer (Biolegend) for 10 min at room temperature and the cell suspension was washed twice with PBS. Cells were kept in PBS with 2 % FBS on until further staining and CyTOF analysis. Spleens were homogenized through a 70 μm cell strainer (BD Biosciences), washed with 4 °C cold PBS, and red blood cell lysis for 3 min at RT using 1 × RBC lysis buffer (Biolegend). Splenocytes were washed with PBS and kept in PBS with 2 % FCS and kept on ice until further staining and CyTOF analysis. Both lobes of a lung were rinsed with ice-cold PBS and transferred to a gentleMACS C tube (Miltenyi Biotec) and digested with 2 mg/mL collagenase D and 80 U/mL DNase I for 30 min at 37 °C on a gentleMACS Dissociator (Miltenyi Biotec). After digestion, lung cells were kept on ice in PBS with 2 % FBS until further staining and CyTOF analysis. The liver was dissected and homogenized through a 100 μm cell strainer (BD Biosciences). After washing in PBS, the liver cell pellet was resuspended in 10 mL of 37.5 % percoll solution and centrifuged at 900g for 25 min without acceleration and brake. The cell pellet was collected, washed with PBS, and kept on ice in PBS with 2 % FBS until further staining and CyTOF analysis.

MIBI-TOF

For the in vivo MIBI-TOF analysis 3 male C57BL/6J (cat.# 000664) mice per group were used. Mice were injected I.V. retro-orbitally with a 100 μL cocktail of TMDs (MoS₂ and WS₂), 20 mg/g each in sterile PBS) or only sterile PBS. After 24 h mice were euthanized by CO₂ inhalation followed by blood withdrawal via cardiac puncture before organ and tissue dissection. Spleen, Liver, Lungs, and Kidneys were harvested and fixed for 24 h in a solution containing paraformaldehyde (PFA) 4 %. After 24 h fixation, organs were washed and kept in 70 % EtOH before paraffin embedding.

Antibody conjugation

Metal conjugated primary antibodies were prepared as described previously [60], using antibody conjugation kits from Ionpath Inc.

MIBI-TOF staining

Staining was performed as previously described [61]. Briefly, tissue Section (4 μm thick) were cut from FFPE tissue blocks and mounted on silanized-gold slides (Ionpath Inc.). Slide-tissue sections were baked at 70 ℃ for 20 min. Tissue sections were deparaffinized with 3 washes of fresh-xylene. Tissue sections were then rehydrated with successive washes of ethanol 100 % (2×), 95 % (2×), 80 % (1×), 70 % (1×), and distilled water. Washes were performed using a Leica ST4020 Linear Stainer (Leica Biosystems, Wetzlar, Germany) The sections were then immersed in epitope retrieval buffer (Antigen Retrieval Solution, Tris-EDTA, pH 9, abcam) and incubated at 97 C for 40 min using Lab vision PT module (Thermofisher Scientific, Waltham, MA). Slides were washed with TBS with Tween 20 buffer (TBST, Ionpath Inc.). Sections were then blocked for 1 h with 3 % (v/v) donkey serum (Sigma-Aldrich, St Louis, MO). Metal-conjugated antibody mix was prepared in 3 % (v/v) donkey serum as previously reported [28], and filtered using centrifugal

filter, 0.1 μm PVDF membrane (Ultrafree-MC, Merck Millipore, Tullagreen Carrigtowhill, Ireland). Two panels of antibody mix were prepared: with the first, slides were incubated overnight at 4 ℃ in a humid chamber; and with the second, slides were incubated the next morning for 1 h at room temperature. Slides were then washed twice for 5 min in TBST wash buffer and fixed for 5 min in diluted glutaraldehyde solution 2 % (Electron Microscopy Sciences, Hatfield, PA) in PBS-low barium. Tissue sections were then dehydrated with successive washes of Tris 0.1 M (pH 8.5), (3×), distilled water (2×), and ethanol 70 % (1×), 80 % (1×), 95 % (2×), 100 % (2×). Slides were immediately dried in a vacuum chamber for at least 1 h prior to imaging.

Imaging and image processing

Imaging was performed using the MIBIscope system (Ionpath Inc.). TMDs signal was detected for Tungsten and Molybdenum at the $^{180-186}$W and ^{95}Mo channels respectively. Following image acquisition, output multi-dimensional TIFF images were processed for background subtraction, noise removal, and aggregate removal using MAUI [62].

Statistical analysis

All values are expressed as mean ± S.D. Comparison between groups was performed by one-way ANOVA, followed by Tukey's post hoc multiple comparison where data was normally distributed. Data that did not follow the normal distribution were statistically analyzed by Kruskall-Wallis ANOVA. Comparisons between the two groups were performed using a two-tailed Student's t-test. A value of $p < 0.05$ was considered significant.

CRediT authorship contribution statement

L.G.D. conceived the project and coordinated the study. A.G., L.F., and L.G.D., wrote the manuscript, to which all authors contributed. C.C. coordinated the nanomaterial production and characterization. Y.S. synthesized and characterized the materials. A.G., L.F., M.O., and S.K. performed the experiments and analyzed the data. L.K. and O.F. performed MIBI-TOF. B.D. coordinated the Luminex and RNA-seq analysis. J-C. G. performed Luminex and analyzed the data. A.G., L.F., M.O., D.B., B.F., and L.G.D. interpreted the experimental data, to which all the authors contributed.

Declaration of Competing Interest

The authors declare the following financial interests/personal relationships which may be considered as potential competing interests: Lucia Gemma Delogu (corresponding author), Laura Fusco (co-author) has patent pending to University of Padua.

Data availability

Data will be made available on request.

Acknowledgments

Appendix A. Supporting information

Supplementary data associated with this article can be found in the online version at doi:10.1016/j.nantod.2023.102084.

References

[1] P.T.K. Loan, W. Zhang, C.-T. Lin, K.-H. Wei, L.-J. Li, C.-H. Chen, Adv. Mater. 26 (2014) 4838.
[2] W. Choi, N. Choudhary, G.H. Han, J. Park, D. Akinwande, Y.H. Lee, Mater. Today 20 (2017) 116.
[3] X. Li, J. Shan, W. Zhang, S. Su, L. Yuwen, L. Wang, Small 13 (2017).
[4] S. Niknam, S.A. Dehdast, O. Pourdakan, M. Shabani, M.K. Koohi, Nanomed. Res. J. 7 (2022) 214.
[5] L. Fusco, A. Gazzi, G. Peng, Y. Shin, S. Vranic, D. Bedognetti, F. Vitale, A. Yilmazer, X. Feng, B. Fadeel, C. Casiraghi, L.G. Delogu, Theranostics 10 (2020) 5435.
[6] J.-W. Choi, J. Yoon, J. Lim, M. Shin, S.-N. Lee, Materials (Basel) 14 (2021) 518.
[7] B. Fadeel, L. Farcal, B. Hardy, S. Vazquez-Campos, D. Hristozov, A. Marcomini, I. Lynch, E. Valsami-Jones, H. Alenius, K. Savolainen, Nat. Nanotechnol. 13 (2018) 537.
[8] G. Peng, B. Fadeel, Adv. Drug Deliv. Rev. 188 (2022), 114422.
[9] W.Z. Teo, E.L.K. Chng, Z. Sofer, M. Pumera, Chem. – A Eur. J. 20 (2014) 9627.
[10] X. Wang, N.D. Mansukhani, L.M. Guiney, Z. Ji, C.H. Chang, M. Wang, Y.-P. Liao, T.-B. Song, B. Sun, R. Li, T. Xia, M.C. Hersam, A.E. Nel, Small 11 (2015) 5079.
[11] J. Li, L.M. Guiney, J.R. Downing, X. Wang, C.H. Chang, J. Jiang, Q. Liu, X. Liu, K. C. Mei, Y.P. Liao, T. Ma, H. Meng, M.C. Hersam, A.E. Nel, T. Xia, Small 17 (2021).
[12] G. Peng, S. Keshavan, L. Delogu, Y. Shin, C. Casiraghi, B. Fadeel, Small 18 (2022), 2107816.
[13] H. Lin, D.-K. Ji, M.A. Lucherelli, G. Reina, S. Ippolito, P. Samorì, A. Bianco, Small 16 (2020), 2002194.
[14] H. Lin, S. Peng, S. Guo, B. Ma, M.A. Lucherelli, C. Royer, S. Ippolito, P. Samorì, A. Bianco, Small 18 (2022), 2107652.
[15] P. Yang, S. Ke, L. Tu, Y. Wang, S. Ye, S. Kou, L. Ren, ACS Biomater. Sci. Eng. 6 (2020) 1764.
[16] H. Lin, Z. Song, A. Bianco, J. Environ. Sci. Health Part B 56 (2021) 333.
[17] Z. Gu, S.H. Chen, Z. Ding, W. Song, W. Wei, S. Liu, G. Ma, R. Zhou, Nanoscale 11 (2019) 22293.
[18] L. Deng, X. Pan, Y. Zhang, S. Sun, L. Lv, L. Gao, P. Ma, H. Ai, Q. Zhou, X. Wang, L. Zhan, IJN 15 (2020) 2971.
[19] P. Yuan, X. Hu, Q. Zhou, Nanotoxicology 14 (2020) 1137.
[20] W. Xie, J. Lu, Z. Guo, X. Guo, Y. Chi, J. Ye, J. Zhang, W. Xu, L. Zhao, Y. Wei, Nano Res. 15 (2022) 2244.
[21] Q. Han, X. Wang, X. Jia, S. Cai, W. Liang, Y. Qin, R. Yang, C. Wang, Nanoscale 9 (2017) 5927.
[22] Y.-S.S. Yang, P.U. Atukorale, K.D. Moynihan, A. Bekdemir, K. Rakhra, L. Tang, F. Stellacci, D.J. Irvine, Nat. Commun. 8 (2017), 14069.
[23] F.J. Hartmann, S.C. Bendall, Nat. Rev. Rheuma 16 (2020) 87.
[24] M.H. Spitzer, G.P. Nolan, Cell 165 (2016) 780.
[25] L. Keren, M. Bosse, S. Thompson, T. Risom, K. Vijayaragavan, E. McCaffrey, D. Marquez, R. Angoshtari, N.F. Greenwald, H. Fienberg, J. Wang, N. Kambham, D. Kirkwood, G. Nolan, T.J. Montine, S.J. Galli, R. West, S.C. Bendall, M. Angelo, Sci. Adv. 5 (2019), eaax5851.
[26] M.K. Ha, S.J. Kwon, J.-S. Choi, N.T. Nguyen, J. Song, Y. Lee, Y.-E. Kim, I. Shin, J.-W. Nam, T.H. Yoon, Small 16 (2020), e1907674.
[27] M. Orecchioni, D. Bedognetti, L. Newman, C. Fuoco, F. Spada, W. Hendrickx, F. M. Marincola, F. Sgarrella, A.F. Rodrigues, C. Ménard-Moyon, G. Cesareni, K. Kostarelos, A. Bianco, L.G. Delogu, Nat. Commun. 8 (2017), 1109.
[28] L. Fusco, A. Gazzi, C.E. Shuck, M. Orecchioni, D. Alberti, S.M. D'Almeida, D. Rinchai, E. Ahmed, O. Elhanani, M. Rauner, B. Zavan, J.-C. Grivel, L. Keren, G. Pasqual, D. Bedognetti, K. Ley, Y. Gogotsi, L.G. Delogu, Adv. Mater. (2022), e2205154.
[29] W. Yan, A. Rafieerad, K.N. Alagarsamy, L.R. Saleth, R.C. Arora, S. Dhingra, Nano Today 48 (2023), 101706.
[30] D. McManus, S. Vranic, F. Withers, V. Sanchez-Romaguera, M. Macucci, H. Yang, R. Sorrentino, K. Parvez, S.-K. Son, G. Iannaccone, K. Kostarelos, G. Fiori, C. Casiraghi, Nat. Nanotech. 12 (2017) 343.

[31] Y. Shin, S. Vranic, X. Just-Baringo, S.M. Gali, T. Kisby, Y. Chen, A. Gkoutzidou, E. Prestat, D. Beljonne, I. Larrosa, K. Kostarelos, C. Casiraghi, Nanoscale 12 (2020) 12383.

[32] E. Landhuis, Nature 557 (2018) 595.

[33] M. Orecchioni, V. Bordoni, C. Fuoco, G. Reina, H. Lin, M. Zoccheddu, A. Yilmazer, B. Zavan, G. Cesareni, D. Bedognetti, A. Bianco, L.G. Delogu, Small 16 (2020) 2070117.

[34] C. Fuoco, X. Luan, L. Fusco, F. Riccio, G. Giuliani, H. Lin, M. Orecchioni, C. Martín, G. Cesareni, X. Feng, Y. Mai, A. Bianco, L.G. Delogu, Appl. Mater. Today 29 (2022), 101593.

[35] C.-X. Hu, Y. Shin, O. Read, C. Casiraghi, Nanoscale 13 (2021) 460.

[36] O. Read, Y. Shin, C. Hu, M. Zarattini, M. Boyes, X. Just-Baringo, A. Panigrahi, I. Larrosa, C. Casiraghi, Carbon 186 (2022) 550.

[37] H. Yang, Y. Hernandez, A. Schlierf, A. Felten, A. Eckmann, S. Johal, P. Louette, J.-J. Pireaux, X. Feng, K. Mullen, V. Palermo, C. Casiraghi, Carbon 53 (2013) 357.

[38] H. Yang, F. Withers, E. Gebremedhn, E. Lewis, L. Britnell, A. Felten, V. Palermo, S. Haigh, D. Beljonne, C. Casiraghi, 2D Mater. 1 (2014), 011012.

[39] S.P. Mukherjee, N. Lozano, M. Kucki, A.E. Del Rio-Castillo, L. Newman, E. Vázquez, K. Kostarelos, P. Wick, B. Fadeel, PLoS One 11 (2016), e0166816.

[40] L. Fusco, M. Pelin, S. Mukherjee, S. Keshavan, S. Sosa, C. Martín, V. González, E. Vázquez, M. Prato, B. Fadeel, A. Tubaro, Carbon 159 (2020) 598.

[41] R. Kurapati, L. Muzi, A.P.R. de Garibay, J. Russier, D. Voiry, I.A. Vacchi, M. Chhowalla, A. Bianco, Adv. Funct. Mater. 27 (2017), 1605176.

[42] F.T. Andón, S.P. Mukherjee, I. Gessner, L. Wortmann, L. Xiao, K. Hultenby, A. A. Shvedova, S. Mathur, B. Fadeel, Carbon 113 (2017) 243.

[43] C. Moore, A. Harvey, J.N. Coleman, H.J. Byrne, J. McIntyre, 2D Mater. 7 (2020), 025003.

[44] C. Moore, D. Movia, R.J. Smith, D. Hanlon, F. Lebre, E.C. Lavelle, H.J. Byrne, J. N. Coleman, Y. Volkov, J. McIntyre, 2D Mater. 4 (2017), 025065.

[45] Q. Liu, S. Tomei, M.L. Ascierto, V. De Giorgi, D. Bedognetti, C. Dai, L. Uccellini, T. Spivey, Z. Pos, J. Thomas, J. Reinboth, D. Murtas, Q. Zhang, L. Chouchane, G. R. Weiss, C.L. Slingluff, P.P. Lee, S.A. Rosenberg, H. Alter, K. Yao, E. Wang, F. M. Marincola, J. Clin. Invest. 124 (2014) 2147.

[46] D. Bedognetti, T.L. Spivey, Y. Zhao, L. Uccellini, S. Tomei, M.E. Dudley, M. L. Ascierto, V. De Giorgi, Q. Liu, L.G. Delogu, M. Sommariva, M.R. Sertoli, R. Simon, E. Wang, S.A. Rosenberg, F.M. Marincola, Br. J. Cancer 109 (2013) 2412.

[47] M. Pardo, T. Shuster-Meiseles, S. Levin-Zaidman, A. Rudich, Y. Rudich, Environ. Sci. Technol. 48 (2014) 3457.

[48] R. Jin, J. Yang, P. Ding, C. Li, B. Zhang, W. Chen, Y.-D. Zhao, Y. Cao, B. Liu, Nanotechnology 31 (2020), 205102.

[49] Y.-S. Wang, X.-J. Li, W.-O. Zhao, Bosn. J. Basic Med. Sci. 12 (2012) 94.

[50] S.J. Mayr, R.-R. Mendel, G. Schwarz, Biochim. Biophys. Acta Mol. Cell Res. 1868 (2021), 118883.

[51] M. Cao, R. Cai, L. Zhao, M. Guo, L. Wang, Y. Wang, L. Zhang, X. Wang, H. Yao, C. Xie, Y. Cong, Y. Guan, X. Tao, Y. Wang, S. Xu, Y. Liu, Y. Zhao, C. Chen, Nat. Nanotechnol. 16 (2021) 708.

[52] B. Pulendran, M.M. Davis, Science 369 (2020), eaay4014.

[53] Y. Shin, X. Just-Baringo, M. Zarattini, L.H. Isherwood, A. Baidak, K. Kostarelos, I. Larrosa, C. Casiraghi, Mol. Syst. Des. Eng. 4 (2019) 503.

[54] U. Khan, A. O'Neill, M. Lotya, S. De, J.N. Coleman, Small 6 (2010) 864.

[55] M. Lotya, Y. Hernandez, P.J. King, R.J. Smith, V. Nicolosi, L.S. Karlsson, F. M. Blighe, S. De, Z. Wang, I.T. McGovern, G.S. Duesberg, J.N. Coleman, J. Am. Chem. Soc. 131 (2009) 3611.

[56] M. Lotya, P.J. King, U. Khan, S. De, J.N. Coleman, ACS Nano 4 (2010) 3155.

[57] J.N. Coleman, M. Lotya, A. O'Neill, S.D. Bergin, P.J. King, U. Khan, K. Young, A. Gaucher, S. De, R.J. Smith, I.V. Shvets, S.K. Arora, G. Stanton, H.-Y. Kim, K. Lee, G.T. Kim, G.S. Duesberg, T. Hallam, J.J. Boland, J.J. Wang, J.F. Donegan, J. C. Grunlan, G. Moriarty, A. Shmeliov, R.J. Nicholls, J.M. Perkins, E.M. Grieveson, K. Theuwissen, D.W. McComb, P.D. Nellist, V. Nicolosi, Science 331 (2011) 568.

[58] S.P. Mukherjee, K. Kostarelos, B. Fadeel, Adv. Health Mater. 7 (2018).

[59] F.T. Andãn, S.P. Mukherjee, I. Gessner, L. Wortmann, L. Xiao, K. Hultenby, A. A. Shvedova, S. Mathur, B. Fadeel, Carbon (2017).

[60] S.C. Bendall, E.F. Simonds, P. Qiu, E.D. Amir, P.O. Krutzik, R. Finck, R.V. Bruggner, R. Melamed, A. Trejo, O.I. Ornatsky, R.S. Balderas, S.K. Plevritis, K. Sachs, D. Pe'er, S.D. Tanner, G.P. Nolan, Science (New York, N.Y.) 332 (2011) 687.

[61] L. Keren, M. Bosse, D. Marquez, R. Angoshtari, S. Jain, S. Varma, S.-R. Yang, A. Kurian, D. Van Valen, R. West, S.C. Bendall, M. Angelo, Cell 174 (2018) 1373.

[62] A. Baranski, I. Milo, S. Greenbaum, J.-P. Oliveria, D. Mrdjen, M. Angelo, L. Keren, PLOS Comput. Biol. 17 (2021), e1008887.